Sensing Inhalation Injury-Associated Changes in Airway Wall Compliance by Anatomic Optical Coherence Elastography

Ruofei Bu [ID], Santosh Balakrishnan [ID], Nicusor Iftimia, Hillel Price [ID], Carlton Zdanski [ID], Sorin Mitran, and Amy L. Oldenburg [ID]

Abstract—**Quantitative methods for assessing the severity of inhalation (burn) injury are needed to aid in treatment decisions. We hypothesize that it is possible to assess the severity of injuries on the basis of differences in the compliance of the airway wall. Here, we demonstrate the use of a custom-built, endoscopic, anatomic optical coherence elastography (aOCE) system to measure airway wall compliance. The method was first validated using airway phantoms, then performed on *ex vivo* porcine tracheas under varying degrees of inhalation (steam) injury. A negative correlation between aOCE-derived compliance and severity of steam injuries is found, and spatially-resolved compliance maps reveal regional heterogeneity in airway properties.**

Index Terms—**Biomedical engineering, biomedical imaging, elastography, optical coherence tomography, optical imaging.**

I. INTRODUCTION

INHALATION injury is one of the most critical injuries to humans with thermal burns or smoke inhalation, occurring in approximately 10-20% of burn patients [1], [2]. It is associated with a 10-30% mortality rate and results in nearly 10,000 deaths annually [1], [3]. Such injuries can lead to severe complications including edema, irritation, increased microvascular permeability, loss of ciliary action and airway obstruction [4], [5]. Reduced lung compliance, increased airway resistance, and abnormal compliance in upper airways are also observed in many patients after inhalation injury or endotracheal intubation [6]–[8]. To diagnose inhalation injury, assessing the severity of injuries is crucial, as it can be considered one of the main contributing factors to mortality for thermal-injured patients [5], [9]. Currently there is no standard for severity grading in inhalation injury; new tools which can assess severity of injury are needed to guide decision-making for appropriate management without unnecessary ventilation or drug therapy, thereby preventing secondary injuries [10], [11]. Such tools could also be used to follow efficacy of treatment and guide intervention.

To stratify inhalation injury severity, several techniques have been developed and utilized. At present, the combination of fiberoptic bronchoscopy (FOB) and histology is considered the gold standard for early evaluation of inhalation injuries [12]. However, FOB is subjective, and histology is limited to biopsied tissues. Computed tomography (CT) [13] and ventilation/perfusion scintigraphy [9] have also been used for airway injury assessment, but lack information about airway elastic properties. Elastography of the airway by magnetic resonance elastography (MRE) [14] and endobronchial ultrasound elastography (EBUS) [15] may be possible but are technically challenging due to limited spatial resolution and speed for capturing minute airway wall deformations.

To address the need for improved airway injury stratification, here we propose to employ anatomic optical coherence elastography (aOCE) to quantify burn-induced changes in airway wall compliance. aOCE is based upon optical coherence tomography (OCT), which provides micrometer-resolution, depth-resolved imaging via non-invasive near-infrared light, and is readily adapted to a fiber-optic for endoscopic imaging [16]. For imaging of larger luminal organs such as upper airways, long-range or anatomic OCT (aOCT) is employed to capture the air-tissue interface and quantify the luminal geometry [17], [18]. As relevant to airway injury, aOCT has been utilized for assessing airway mucosal thickening in response to smoke inhalation injury in rabbits [19], [20]. Importantly, aOCT offers sufficient spatial resolution and speed to capture airway wall deformation during respiration and to subsequently compute wall compliance. This

Ruofei Bu and Santosh Balakrishnan are with the Department of Biomedical Engineering, University of North Carolina at Chapel Hill.

Nicusor Iftimia is with the Physical Sciences Inc., New England Business Center.

Hillel Price is with the Department of Physics and Astronomy, University of North Carolina at Chapel Hill.

Carlton Zdanski is with the Department of Otolaryngology/Head and Neck Surgery, University of North Carolina at Chapel Hill.

Sorin Mitran is with the Department of Mathematics, University of North Carolina at Chapel Hill.

Amy L. Oldenburg is with the Department of Biomedical Engineering, with the Department of Physics and Astronomy and Biomedical Research Imaging Center, and also with the University of North Carolina at Chapel Hill, Chapel Hill, NC 27599-3216 USA (e-mail: aold@physics.unc.edu).

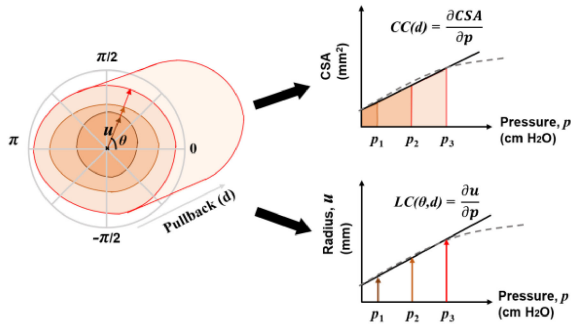Digital Object Identifier 10.1109/TBME.2020.3037288

Fig. 1. Concept diagram of an airway lumen expanding under increasing pressure (left) and corresponding measurements of CC and LC based on OCT measurements of the air-lumen interface at each pressure.

Fig. 2. (a) Diagram of phantoms of inner radius r and wall thickness Δr. Phantom A is a simple tube, and phantom B is notched with regions outside and inside the notch indicated by B1 and B2, respectively. Dimensions are provided in Table I. (b) Predicted phantom deformation from minimum to maximum pressure ($p_{\min}$ to $p_{\max}$) via the finite element model. At $p_{\min}$ only the phantom's inner surface is displayed, for ease of comparison.

TABLE I
PROPERTIES OF PHANTOMS*

Phantom	A	B1	B2
Inner Radius (r, mm)	9.34 ± 0.20	9.32 ± 0.33	
Thickness (Δr, mm)	1.56 ± 0.06	1.39 ± 0.29	0.54 ± 0.17
Angle (θ, degree)	360	0-333	333-360
Young's modulus (kPa)	275 ± 6	275 ± 6	
CC (predicted, mm²/cm H₂O)	1.11 ± 0.04	1.62 (from FEM)	
LC (predicted, mm/cm H₂O)	0.019 ± 0.001	depends on θ	

*All data are presented as mean ± standard deviation.

offers the novel ability for airway wall elastography by aOCE, first demonstrated in a study of obstructive airway disorders [18], [21]. Recent efforts adapting aOCE to a swept-source system with higher scan rates have even revealed the viscoelastic nature of *in vivo* airways [22].

Our past efforts have focused on phantom and *ex vivo* tissue validation of aOCT for accurately segmenting airway lumen [23], [24], then subsequently validation of aOCE by sweeping the intraluminal pressure and quantifying wall compliance [25], [26]. An important aspect of the latter is the use of a pressure catheter in conjunction with the aOCT probe to accurately measure the pressure *in situ*. aOCE measurements include cross-sectional compliance (CC) that provides one value for each airway cross-section, and local compliance (LC) that is spatially resolved over the circumference of the airway. In [26], we found that LC correlated with the tracheal ring structure of *ex vivo* pig airways, however, our prior studies did not evaluate LC along the length of the airway. Here, we perform aOCE scans along the airway, and present LC as a 2D compliance map that enables visualization of the spatially-resolved wall compliance over the entire scanned airway luminal surface. First, we employ elastic tube phantoms to validate aOCE-derived compliance against an analytical model (for perfect tubes) and a finite element model (for tubes with a notch). Then, we employ aOCE to measure CC and LC in *ex vivo* pig tracheas before and after steam injury. Here we chose to employ injury via steam with different exposure times as a simplified and controlled method for simulating inhalation injury. This allowed us to assess elastic changes in airways as a function of injury severity.

II. METHODS

The compliance measurements obtained in this study are CC and LC. CC provides a single measurement at each cross-sectional slice, and can be used to locate abnormalities along the length of airway; in contrast, LC maps the pattern of compliance over the entire airway luminal surface. For CC and LC measurements, constant pressure at different levels is utilized, so the measured luminal geometry at one transverse position can be registered to the same location within one frame. As shown in Fig. 1, the CC and LC (at angle θ) at one pullback position
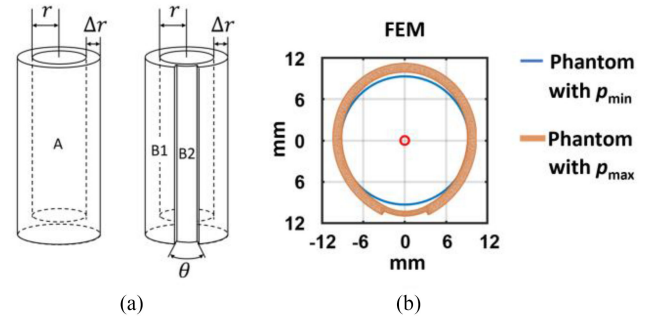
(d) are defined as the derivative of cross-sectional area (CSA) and radius (u), respectively, with respect to pressure (p):

$$CC\ (d) = \frac{\partial CSA\ (d)}{\partial p} \qquad (1)$$

$$LC\ (\theta, d) = \frac{\partial u\ (\theta, d)}{\partial p} \qquad (2)$$

A. Sample Preparation

1) Elastic Phantoms: Two phantoms made from polydimethylsiloxane (PDMS, concentration elaborated in previous study[26]) were designed and fabricated to mimic the inner radius, CC, and LC of tracheas (Fig. 2(a)) [26]. Phantoms had Al_2O_3 powder added to provide light scattering for OCT. Phantom A was a cylindrical tube with uniform wall thickness, and Phantom B was similar to Phantom A but with a notch along the length of the tube to provide non-uniform LC. The dimensions of the two phantoms are summarized in Table I. Their Young's moduli were measured with a commercial texture analyzer (TA.XT Plus, Texture Technologies, Scarsdale,
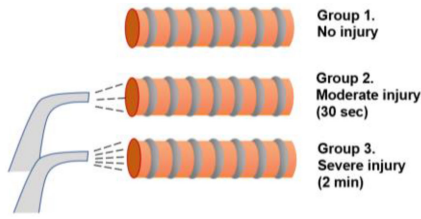
Fig. 3. Different levels of steam exposure applied to *ex vivo* pig tracheas.

NY). The theoretical values of CC and LC of phantom A were computed using a thick-walled tube model described previously [26] and are reported in Table I. For Phantom B, due to its non-uniform thickness, a finite-element model (FEM), also described in [26], was employed to predict the deformation of the phantom (Fig. 2(b)). The method was implemented with the FreeFEM software by simulating the deformation of the phantom under different pressures. The exported coordinates of each point on the interior surface of the phantom before/after deformation were subsequently used to compute CC which is constant along the length of the tube (Table I), and to generate plots of the LC is a function of angle as shown in the results.

2) Ex Vivo Pig Tracheas: Nine tracheas ($N = 9$) were dissected from domestic pigs and frozen for storage. Before experiments, they were thawed to room temperature, and cannulated using endotracheal tubes (ETT). A commercial steam cleaner (I500b, Reliable Corp) was used to produce steam injuries inside the tracheas with 50 psi operating pressure at 105°C. The assembled nozzle of the cleaner was placed at the front end of the ETT. The exposure time of the steam was used to vary the severity of steam injury, as shown in Fig. 3. The tracheas were randomly assigned to three groups: tracheas with no injury (or "pseudo-injury"), which are considered as the control group ($N_1 = 3$), tracheas exposed to steam for 30 seconds, which are considered as those with moderate injury ($N_2 = 3$), and tracheas exposed to steam for 2 minutes, which are considered as those with severe injury ($N_3 = 3$). Each trachea in groups 2 or 3 was scanned with aOCT before any injury was caused, and then moved away from the imaging area to be exposed to steam. After cooling down to room temperature, each trachea was moved back for imaging. Tracheas in the control group were processed and imaged following the same procedures, except no steam sprayed out of the steamer.

B. aOCE System Setup

A custom-built aOCE system which incorporates an intraluminal pressure catheter, as described in detail in [25], was used to capture the luminal deformation of airway phantoms and *ex vivo* tracheas under varying pressure, and subsequently compute wall compliance (CC and LC). Designed for endoscopic imaging of airways, the system employs a fiber-optic catheter imaging probe of 0.86 mm outer diameter (including the protective sheath) with a side-reflected laser beam. The wavelength-swept laser source (SL1310V1, Thorlabs Inc.) has a central wavelength of 1310 nm and sweep rate of 100 kHz, providing an axial resolution

of 12.6 μm and axial imaging range of 12 mm. The fiber optic catheter is distally scanned with a rotation rate of 20 Hz and pullback speed of 6 mm/s. The pullback distance is 80 mm for phantom scans, and 50 mm for trachea scans. A ventilator (SERVO 900C, Siemens-Elema AB) is used to provide positive pressure to phantoms and airways, and is run in continuous positive airway pressure (CPAP) mode. To measure compliance in phantoms, aOCT scans with 80 mm pullback under 3 or 4 levels of static pressure were performed. The pressure level was set to be 6, 12, 18 or 24 cm H_2O. The maximum pressure of 24 cm H_2O was applied on both phantoms and tracheas, but not accounted for in the analysis of trachea scans, as it was beyond the linear region of the CSA versus pressure curve. The pressure catheter (SPR-330A, Millar Inc.) measures the *in situ* pressure simultaneously right next to the aOCT catheter and was positioned centimeters proximally from the catheter tip to avoid blocking the view of aOCT.

C. Imaging and Analysis Protocol

At the beginning of each scan, both the aOCT and pressure catheters were inserted via an ETT into the prepared phantoms or tracheas, and the aOCT catheter was approximately centered along the trachea to minimize distortion and other artifacts. Then, aOCT pullback scans were performed with pressure data simultaneously digitized. The helically-scanned airway lumen from each aOCT scan was later resampled into Cartesian space, and a semi-automated segmentation method was used to segment the air-tissue interface. The results were used to calculate the displacement as a function of θ and d, and the CSA was calculated by numerically integrating the distance of the airway wall from the center over θ according to methods described in [24]. CC was then computed at each pullback position by the slope of a linear regression fit of CSA versus pressure as defined in Eqn. (1). To compute LC of tracheas, aOCT images under different pressure levels were aligned manually in both longitudinal and circumferential directions, using the tracheal bronchus and the trachealis muscles as landmarks. LC was then computed at each polar angle and pullback position by the slope of a linear regression fit of radius versus pressure as defined in Eqn. (2). Here, radius is defined relative to the dynamic centroid of the lumen area, as this method was shown to provide the most stable measurements of LC under tissue deformation [26].

For the steam injury study, as compliance varies between tracheas, both CC and LC cannot be easily normalized to be compared. Thus, instead of analyzing the mean values for each group, we investigated the relative change of compliance pre and post injury per trachea, then averaged within each group. Specifically, pullback scans under different pressure levels were performed on each trachea (j) before (b) and after (a) injury. CC was then computed for each trachea before injury ($CC_{b,j}(d)$) as a function of pullback position (d) as well as after the injury ($CC_{a,j}(d)$). Then, the percent change of CC was computed at each d for the 3 tracheas of each group according to $\Delta CC_j(d) = \frac{CC_{b,j}(d) - CC_{a,j}(d)}{CC_{b,j}(d)} \times 100$. Statistics were then computed by averaging $CC_{a,j}(d)$, $CC_{b,j}(d)$ and $\Delta CC_j(d)$ across positions (d) and across tracheas (j) within each of the three injury severity
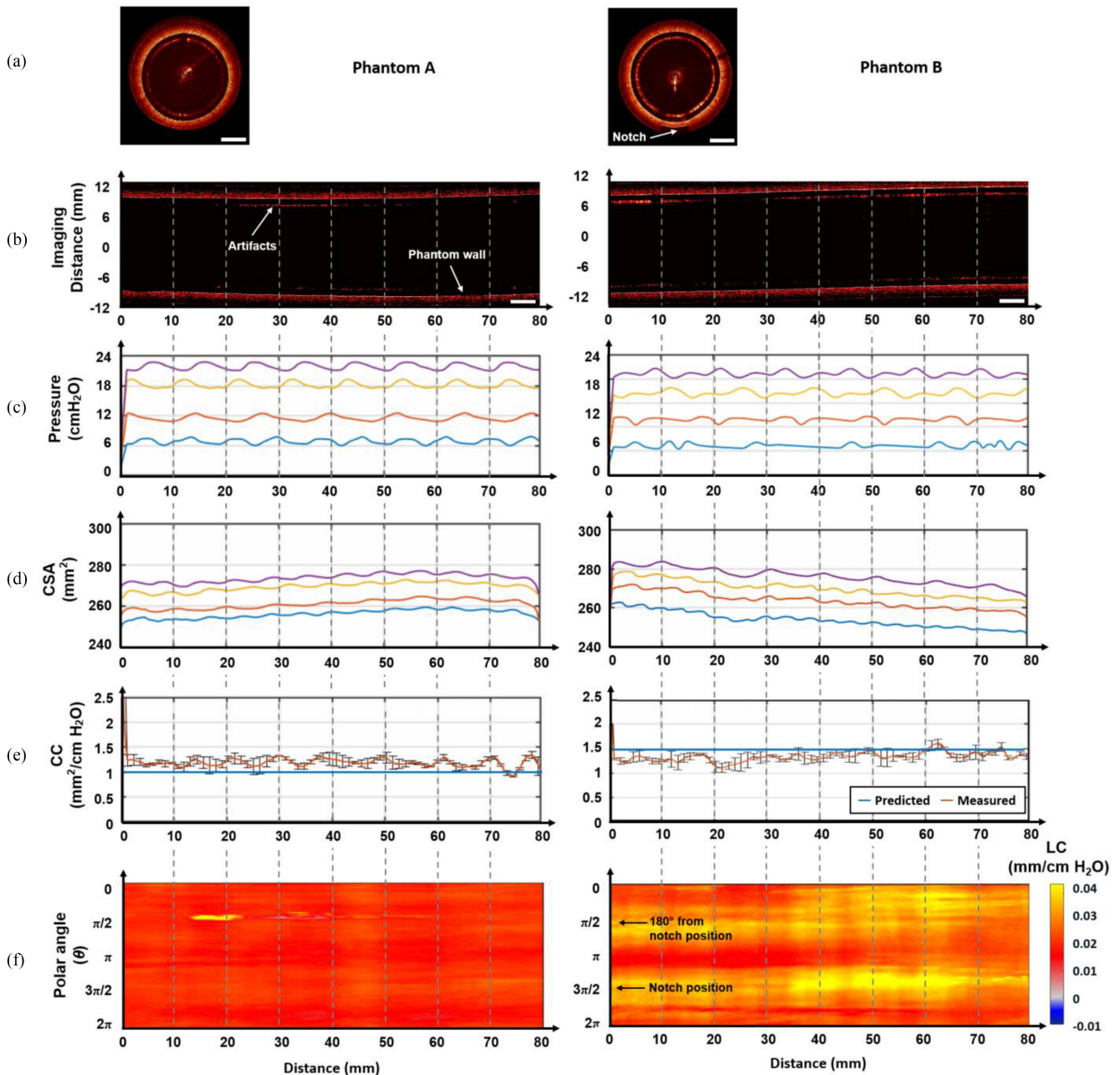
Fig. 4. aOCE results of phantom A and B. (a) aOCT images of the two phantoms in a transverse cross-section; (b) OCT images of the two phantoms in a longitudinal cross-section, where the *x*-coordinate is pullback distance; (c) Measured pressures at the four ventilator pressure settings (nominally 6, 12, 18, and 24 cm H_2O); (d) aOCT-measured CSA vs. pullback distance of each phantom at each corresponding pressure setting of panel (c); (e) Corresponding CC vs. pullback distance derived from the lower 3 pressure settings only; (f) Corresponding LC maps over the luminal surface angle (θ) and pullback distance, displayed as a heat map. Scale bars are 5 mm.

groups. Maps of $LC(\theta,d)$ were also produced from the same data to visualize the heterogeneity of steam injury inside airways.

III. RESULTS

A. aOCE of Elastic Airway Phantoms

1) Phantom With Uniform Thickness (A): Representative aOCT images and measured pressure, CSA and compliance are shown in the left column of Fig. 4. Some imaging artifacts are observed in the aOCT images that are avoided by the segmentation algorithm when determining the air-lumen interface to compute the CSA. The aOCT-measured CC across the pullback distance averaged 1.21 ± 0.36 mm²/cm H_2O, where each of the CSA versus pressure regression lines used to compute CC exhibited an average $R^2 = 0.99 \pm 0.01$. The relatively large variation of CC across pullback distance is primarily attributed to variation in the pressure during the pullback scan due to the ventilator's

TABLE II
aOCT-MEASURED CC OF TRACHEA WITH STEAM INJURY

Tracheas with steam injury	Cross-sectional compliance ($CC_j(d)$, mm²/ cm H₂O)		Change of cross-sectional compliance ($\Delta CC_j(d)$, %)
	Before injury	After injury	
Control			$\dfrac{CC_{a,j}(d) - CC_{b,j}(d)}{CC_{b,j}(d)}$
Moderate	$CC_{b,j}(d)$	$CC_{a,j}(d)$	$\times 100$
Severe			

active feedback adjusting for small sample air leaks when in CPAP mode. Despite the large variation, the mean difference between the measured and theoretical value of CC (1.11 ± 0.04 mm²/cm H₂O) is only 9% and well within experimental error. The corresponding LC map is shown in (f), with the x-axis and y-axis representing the pullback distance and the polar angle, respectively, and the hue showing the measured compliance, with warm colors indicating radial increase (expansion) and cold colors indicating radial decrease (contraction). The LC map, which allows assessment of the spatial pattern of deformation along the airway wall surface, demonstrates good spatial homogeneity as expected in this uniform wall thickness phantom. A small deviation of LC observed in the map (yellow region in Fig. 4f) might be caused by phantom fabrication. The overall LC was 0.018 ± 0.002 mm/cm H₂O with average $R^2 = 0.97 \pm 0.03$ for the fittings of radius versus pressure. The difference between the measured and theoretical LC value of 0.019 ± 0.001 mm/cm H₂O is ~10%. The high average R^2 when computing CC and LC indicate that the phantom exhibits linear elasticity over the $6 - 18$ cm H₂O pressure range used. Differences between the model and experimental results are attributed to imperfections in the mold fabrication process, resulting in a phantom with different dimensions than those used in the model.

2) Phantom With Notch (B): The results of phantom B are presented in Fig. 4 on the right, similarly to those for phantom A. The location of the notch is indicated by an arrow in Fig. 4(a) and corresponds to a polar angle of $3\pi/2$. In Fig. 4(c), a decrease of CSA is observed during pullback, which is attributed to the change of radius of the phantom itself. The decrease arises from imperfection of the mold fabrication and affects the compliance measurements. The measured CC averages 1.93 ± 0.43 mm²/cm H₂O, with $R^2 = 0.97 \pm 0.09$ for the individual regression fits. The difference between the predicted CC of 1.62 mm²/cm H₂O and the measured value is 19%. Both phantom fabrication and pressure fluctuation contributes to this difference. However, the map of LC shows a clear pattern of the heterogeneity of the phantom around $\theta = 3\pi/2$ corresponding to the position of the notch. The average $R^2 = 0.93 \pm 0.06$ for the LC fittings, indicating the reasonable linearity of the measurements.

To understand the spatial pattern of LC observed in Fig. 4(f), we compare the predicted and measured LC versus polar angle, as shown in Fig. 5. The measured LC curve is acquired by averaging LC at all cross sections over the pullback distance. As might be intuitively expected, a larger compliance is observed where the notch is located, due to the locally decreased wall
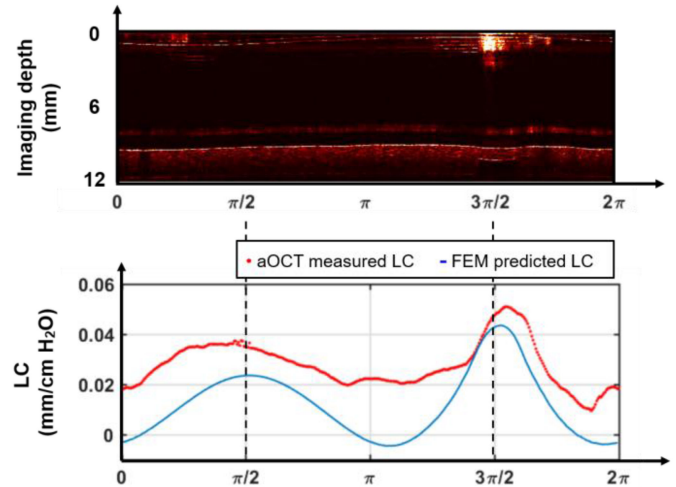

Fig. 5. Comparison of FEM predicted LC and aOCE-derived LC in a notched tube phantom. Top: Raw aOCT image slice (before resampling into Cartesian coordinates, with rotation angle on the horizontal axis and distance from the catheter tip on the vertical axis) with the notch aligned at $\theta = 3\pi/2$. Bottom: plot shows the LC curve in the circumferential direction, with the blue line indicating the predicted values from FEM, and red dots showing the aOCE-derived values.

thickness. Interestingly, a second peak of compliance is also observed at 180° (opposite) the location of the notch, which can be thought of as a folding effect due to the mechanical coupling across the circumference of the tube when under radial stress, and is consistent with our previous findings in a different notched phantom [26].

B. Ex Vivo Pig Tracheas Before and After Steam Injury

Representative aOCE-based CC plots and LC maps of one trachea before and after injury are presented in Fig. 6. Before steam injury, CC was approximately 0.5 mm²/cm H₂O averaged over the 50 mm pullback distance. The extremely large CC near $d = 0$ correlates with the position of the tracheal bronchus, which is used as a landmark for aligning scans under different pressures, and was discarded for CC analysis across tracheas. The LC pattern in the circumferential direction shows two peaks approximately centered at the posterior ($\theta = 3\pi/2$) and anterior ($\theta = \pi/2$) airway. According to the structure of C-shaped cartilage ring, the opening of the airway (comprised of softer trachealis muscle) is located at the posterior airway (marked in Fig. 6e). When the airway deforms, larger displacement/compliance is observed at posterior, as well as anterior airway, producing a pattern similar to that observed in the notched phantom B. The correlation of LC with trachealis muscle at one cross-section has been proven over multiple samples in our previous paper [26]. Interestingly, the LC map shows both longitudinal and circumferential heterogeneity in airway compliance in a ring distributed pattern. This may be related to the distribution of cartilage rings in pig tracheas, or expansion of trachea in the longitudinal direction, but requires further investigation.

After injury, overall CC and LC are both observed to decrease somewhat uniformly throughout the sample. CC reduces to ~0.2
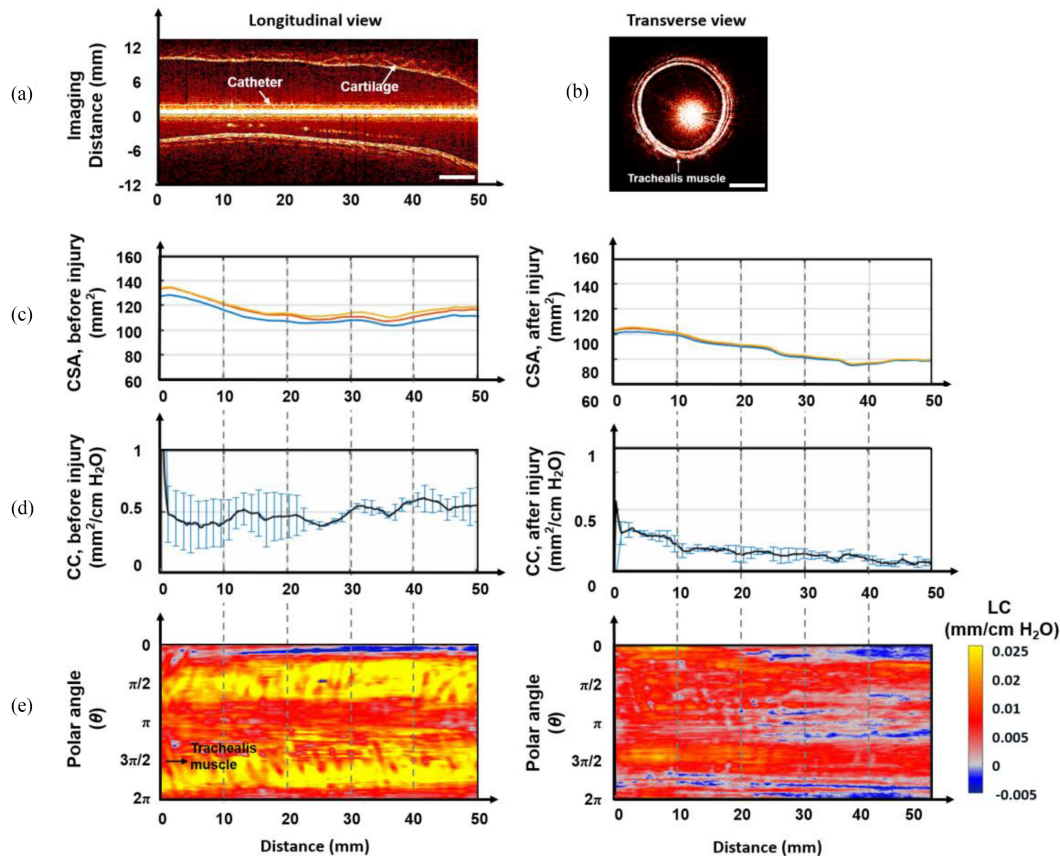
Fig. 6. Representative aOCE of an *ex vivo* trachea before and after steam injury. (a) aOCT image in a longitudinal cross-section; (b) aOCT image in a transverse cross-section (slice); (c) Plots of CSA versus pullback distance before and after steam injury; (d) Corresponding plots of CC before and after steam injury; (e) Corresponding LC map before and after steam injury. Scale bars are 5 mm.
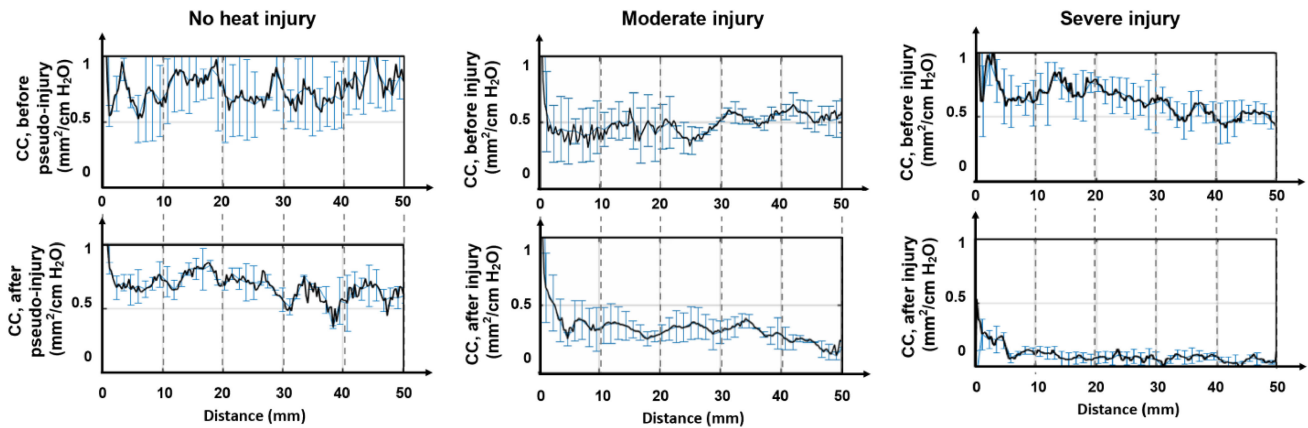

Fig. 7. Representative plots of aOCE-measured CC versus pullback distance before (top row) and after (bottom row) different severities of steam injury. Left: control group; Middle: moderate injury; Right: severe injury. Summarized results across all 3 tracheas of each injury group are provided in Table III.

mm^2/cmH_2O in this trachea, indicating that the tissue has lost most of its ability to deform. A similar phenomenon is observed with the LC map. The overall LC decreases as indicated by the two maps, with maximal compliance of 0.025 mm/cm H_2O before injury dropping to ~0.01 mm/cm H_2O after the injury. The circumferential pattern of larger LC at the posterior and anterior airway also partially disappear.

Example CC plots of tracheas under different severities of injuries are shown in Fig. 7. From left to right, the grade of the steam injury increases from no injury to severe injury. The amount of decrease in CC post-injury is observed to increase with increasing severity of the injury, however noting that the pre-injury value of CC varies from trachea to trachea. Most tracheas have CC ≈ 0.4 – 0.7 mm^2/cm H_2O before injury, which

TABLE III
aOCE-MEASURED CC AND CHANGE OF CC OF *EX VIVO* PIG TRACHEAS
UNDER DIFFERENT SEVERITIES OF STEAM INJURY

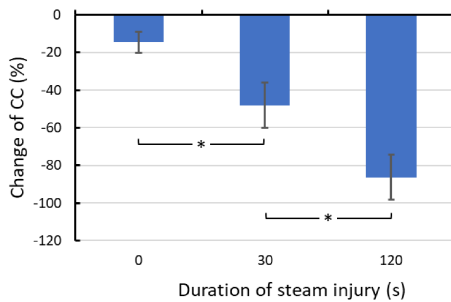| Steam injury severity	Cross-sectional compliance $CC_j(d)$ averaged over d and j, (mm²/ cm H₂O)		Change of cross-sectional compliance $\Delta CC_j(d)$ averaged over d and j (%)
	Before	After	
Control ($n = 3$)	0.40 ± 0.07	0.34 ± 0.06	-14.5 ± 5.7
Moderate ($n = 3$)	0.66 ± 0.26	0.36 ± 0.06	-48.0 ± 11.9
Severe ($n = 3$)	0.66 ± 0.14	0.12 ± 0.05	-86.3 ± 12.0

Fig. 8. Change of CC in *ex vivo* tracheas grouped by the severity of steam injury. *$p < 0.0167$. Error bars represent mean ± standard deviation.

is consistent with prior measurements of compliance of porcine trachea [25].

The results over all tracheas are summarized in Table III. Decreased CC is observed in the groups with steam injuries, with the absolute value of the percent change (ΔCC) increasing with the increased severity of injury. The ΔCC versus injury severity is also plotted in Fig. 8. A significant decrease of compliance is obtained from a two-sample t-test (Bonferroni-adjusted) between tracheas with no/moderate injury and with moderate/severe injury. This indicates that compliance decreases as the severity of the injury increases, and thus the *ex vivo* airway increasingly loses its ability to deform as tissue is more severely burned.

IV. DISCUSSION

Compliance is an extensive property of airways that is dictated by the intensive properties such as the spatial pattern of airway wall elastic modulus and tissue composition, as well as other extensive properties, including lumen geometry and wall thickness. With the measured compliance map, the heterogeneity of airways in both the longitudinal and circumferential directions was revealed. Because our methods here were slightly different than those previous research [26] in that CPAP mode was used instead of pressure-controlled ventilation, we first re-validated the accuracy of pullback-averaged CC and LC measurements using phantoms that mimic both the inner diameter and compliance of typical upper airways. Then, the method was used on *ex vivo* porcine tracheas with and without steam injury to further investigate its ability to assess the severity of injury.

The primary benefits of aOCE are that it is minimally invasive when employed endoscopically, and can be readily adapted for use with other imaging modalities currently employed, namely bronchoscopy. Also, when used in airways, respiratory pressure could be used as an intrinsic source of static/semi-static excitation [27]. Thus, aOCE can be performed to capture displacement in 3D under respiratory pressures and assess airway compliance in real-time. Good agreement between predicted and measured compliance validates the feasibility of our method and the accuracy of aOCE measurement. However, problems still exist with the compliance measurement. For OCT acquisition, general issues like vibration of the probe tip, distortion and segmentation remain. On the clinical side, the gold-standard criteria for diagnosing inhalation injury are age extremes and percent total body surface area, and the treatment is intubation and waiting for injury sequelae such as edema and airway occlusion to subside [28], [29]. The current treatment approach for inhalation injury does not take the nature or extent of injury into consideration. We hypothesize that using the methods described in this paper can be used for stratification of airway injury and aid in appropriate selection of the treatment approach tailored to the extent of the injury. Immediate uses could entail: early assessment/triage of injury severity at remote locations (i.e., forward medical bases on the battlefield or mass casualty events) to determine which patients might benefit from transport to distant advanced medical facilities; and serial examinations to monitor the efficacy of therapies, both standard of care and experimental. At the same time, we recognize that only previously frozen tissues from excised porcine airways were analyzed, and that the freeze/thaw cycle may have changed the viscoelastic properties of the airways studied compared to physiologically intact in vivo airway systems. We also recognize that, changes in elasticity in anatomically and physiologically intact systems might be due to causes other than just thermal damage as in this ex vivo study, but also mechanisms that only occur in living subjects including edema and increased microvascular permeability. In this study, the simplest scenario of steam injury is employed to assess if the method has the potential to be used in diagnosis of inhalation injury. The determination of relative change in compliance in a patient is not easy due to the lack of a pre-injury "ground truth", but over time (possibly with the use of directed studies), normative values for humans could be derived. This would need more experiments on in vivo samples in order to correlate measurements made by aOCT with those derived by another modality (such as CT or MRI) along with clinician derived assessments.

For future clinical study, although the compliance of patients' airways before injuries is not always available, a baseline can be established based on the patient's gender, weight and other features, similar to the pediatric airway atlas for static airway geometry [30]. For highly heterogeneous airway properties, exact localization of damaged airway may require inverse finite element modeling to interpret the relationship between LC and underlying tissue properties. Although with limitations, the change of compliance from expected baseline, or spatial heterogeneity (or lack of) could be used as an index to assess the severity of inhalation injuries.

V. Conclusion

As a new way of displaying heterogeneous aOCE data, here we present for the first time 2D maps of airway wall compliance across the length of phantoms and *ex vivo* pig tracheas. The measurements of phantoms were all within experimental error from theoretical predictions, with a difference of ∼9% and 10% in CC and LC, respectively, of a uniform thickness phantom, and ∼19% in the CC of a notched phantom. The larger error in the notched phantom is primarily attributed to imperfections in the phantom itself, and we expect the capability of aOCE to accurately quantify the true airway wall compliance to within 10%. Furthermore, the circumferential pattern of LC in the notched phantom exhibited two peaks corresponding to the position of the notch and 180° from this position, which were consistent with FEM. Importantly, consistency of compliance along pullback distance is observed when visualizing data in a 2D LC map, validating this new method of visualizing aOCE data.

Using these new methods, we performed aOCE on nine *ex vivo* porcine tracheas. As in our prior study [26], we noted that the anterior and posterior positions of the uninjured tracheas exhibited higher compliance, which is attributed to the posterior position of the incomplete cartilage ring opening and the expected 180° secondary peak due to mechanical coupling across the trachea. These data are now revealed in LC maps, enabling assessment of mechanical features across the entire surface of the airway scanned. Importantly, steam injury resulted in a dramatic decrease in compliance across the length of the airways, with a negative correspondence between the change of CC and the severity of injury. Based on these promising results, the new insight provided by aOCE has the potential to aid in inhalation injury stratification as well as response to therapy and ultimately guide management.

Disclosure

The authors declare that there are no conflicts of interest related to this article.

References

[1] D. N. Herndon, *Total Burn Care*. Philadelphia, PA, USA: Saunders Elsevier, 2007.

[2] P. F. Walker *et al.*, "Diagnosis and management of inhalation injury: An updated review," *Crit. Care*, vol. 19, no. 1, pp. 351–363, Dec. 2015.

[3] K. You *et al.*, "Inhalation injury in burn patients: Establishing the link between diagnosis and prognosis," *Burns*, vol. 40, no. 8, pp. 1470–1475, Dec. 2014.

[4] R. H. Demling, "Smoke inhalation lung injury: An update," *Eplasty*, vol. 8, e27, pp. 254–282, May 2008.

[5] A. C. Miller, E. M. Elamin, and A. F. Suffredini, "Inhaled anticoagulation regimens for the treatment of smoke inhalation–associated acute lung injury," *Crit. Care Med.*, vol. 42, no. 2, pp. 413–419, Feb. 2014.

[6] R. Mlcak *et al.*, "Lung compliance, airway resistance, and work of breathing in children after inhalation injury," *J. Burn Care Rehabil.*, vol. 18, no. 6, pp. 531–534, Nov. 1997.

[7] T. Lund *et al.*, "Upper airway sequelae in burn patients requiring endotracheal intubation or tracheostomy," *Ann. Surg.*, vol. 201, no. 3, pp. 374–382, 1985.

[8] H. A. Gaissert, R. H. Lofgren, and H. C. Grillo, "Upper airway compromise after inhalation injury. Complex strictures of the larynx and trachea and their management," *Ann. Surg.*, vol. 218, no. 5, pp. 672–678, Nov. 1993.

[9] J. A. Moylan *et al.*, "Early diagnosis of inhalation injury using 133 xenon lung scan," *Ann. Surg.*, vol. 176, no. 4, pp. 477–484, Oct. 1972.

[10] L. C. Woodson, "Diagnosis and grading of inhalation injury," *J. Burn Care Res.*, vol. 30, no. 1, pp. 143–145, Jan. 2009.

[11] R. P. Mlcak, O. E. Suman, and D. N. Herndon, "Respiratory management of inhalation injury," *Burns*, vol. 33, no. 1, pp. 2–13, Feb. 2007.

[12] M. J. Masanes *et al.*, "Fiberoptic bronchoscopy for the early diagnosis of subglottal inhalation injury: Comparative value in the assessment of prognosis," *J. Trauma - Inj. Infect. Crit. Care*, vol. 36, no. 1, pp. 59–67, 1994.

[13] H. Yamamura *et al.*, "Computed tomographic assessment of airflow obstruction in smoke inhalation injury: Relationship with the development of pneumonia and injury severity," *Burns*, vol. 41, no. 7, pp. 1428–1434, Nov. 2015.

[14] B. C. Goss *et al.*, "Magnetic resonance elastography of the lung: Technical feasibility," *Magn. Reson. Med.*, vol. 56, no. 5, pp. 1060–1066, Nov. 2006.

[15] J.-H. Jiang, J. F. Turner, and J.-A. Huang, "Endobronchial ultrasound elastography: A new method in endobronchial ultrasound-guided transbronchial needle aspiration," *J. Thorac. Dis.*, vol. 7, no. Suppl 4, pp. S272–S278, Dec. 2015.

[16] G. J. Tearney *et al.*, "In vivo endoscopic optical biopsy with optical coherence tomography," *Science*, vol. 276, no. 5321, pp. 2037–2039, 1997.

[17] J. Armstrong *et al.*, "In vivo size and shape measurement of the human upper airway using endoscopic longrange optical coherence tomography," *Opt. Express*, vol. 11, no. 15, pp. 1817–1826, Jul. 2003.

[18] J. J. Armstrong *et al.*, "Quantitative upper airway imaging with anatomic optical coherence tomography," *Amer. J. Respir. Crit. Care Med.*, vol. 173, no. 2, pp. 226–233, 2006.

[19] J. Yin *et al.*, "In vivo early detection of smoke-induced airway injury using three-dimensional swept-source optical coherence tomography," *J. Biomed. Opt.*, vol. 14, no. 6, 2009, Art. no. 060503.

[20] S.-W. Lee *et al.*, "Quantification of airway thickness changes in smoke-inhalation injury using in-vivo 3-D endoscopic frequency-domain optical coherence tomography," *Biomed. Opt. Express*, vol. 2, no. 2, pp. 243–254, Feb. 2011.

[21] J. P. Williamson *et al.*, "Elastic properties of the central airways in obstructive lung diseases measured using anatomical optical coherence tomography," *Amer. J. Respir. Crit. Care Med.*, vol. 183, no. 5, pp. 612–619, 2011.

[22] S. Balakrishnan *et al.*, "Combined anatomical optical coherence tomography and intraluminal pressure reveal viscoelasticity of the in vivo airway," *J. Biomed. Opt.*, vol. 23, no. 10, pp. 1–4, Oct. 2018.

[23] K. Wijesundara *et al.*, "Quantitative upper airway endoscopy with swept-source anatomical optical coherence tomography," *Biomed. Opt. Express*, vol. 5, no. 3, pp. 788–799, 2014.

[24] H. B. Price *et al.*, "Geometric validation of continuous, finely sampled 3-D reconstructions from aOCT and CT in upper airway models," *IEEE Trans. Med. Imag.*, vol. 38, no. 4, pp. 1005–1015, Apr. 2019.

[25] R. Bu *et al.*, "Airway compliance measured by anatomic optical coherence tomography," *Biomed. Opt. Express*, vol. 8, no. 4, Apr. 2017, Art. no. 2195.

[26] R. Bu *et al.*, "Localized compliance measurement of the airway wall using anatomic optical coherence elastography," *Opt. Express*, vol. 27, no. 12, Jun. 2019, Art. no. 16751.

[27] S. Wang and K. V. Larin, "Optical coherence elastography for tissue characterization: A review," *J. Biophoton.*, vol. 8, no. 4, pp. 279–302, Apr. 2015.

[28] D. J. Dries and F. W. Endorf, "Inhalation injury: Epidemiology, pathology, treatment strategies," scand." *J. Trauma. Resusc. Emerg. Med.*, vol. 21, no. 1, pp. 1–15, Apr. 2013.

[29] D. L. Smith *et al.*, "Effect of inhalation injury, burn size, and age on mortality: A study of 1447 consecutive burn patients," *J. Trauma - Inj. Infect. Crit. Care*, vol. 37, no. 4, pp. 655–659, 1994.

[30] Y. Hong *et al.*, "A pediatric airway atlas and its application in subglottic stenosis," in *Proc. - Int. Symp. Biomed. Imag.*, 2013, pp. 1206–1209.